Investigation of refractive index sensing based on Fano resonance in fiber Bragg grating ring resonators

Carlo Edoardo Campanella,[1] Francesco De Leonardis,[1] Lorenzo Mastronardi,[1] Pietro Malara,[2] Gianluca Gagliardi,[2] and Vittorio M. N. Passaro[1,*]

[1] *Dipartimento di Ingegneria Elettrica e dell'Informazione, Politecnico di Bari Via Edoardo Orabona n. 4, 70125 Bari, Italy*

[2] *Istituto Nazionale di Ottica, Consiglio Nazionale delle Ricerche, via Campi Flegrei, 34 –Comprensorio A. Olivetti, 80078 Pozzuoli (Naples), Italy*

**vittorio.passaro@poliba.it*

Abstract: In this paper we theoretically investigate a ring resonant cavity obtained by closing on itself a π-shifted fiber Bragg grating, to be used for refractive index sensing applications. Differently from a conventional π-shifted fiber Bragg grating, the spectral structure of this cavity is characterized by an asymmetric splitting doublet composed by a right side resonance having an asymmetric Fano profile and a left side resonance having a symmetric Lorentzian profile. The right side resonance shows a narrower and sharper peak than all the other kinds of resonance achievable with both conventional ring resonators and π-shifted fiber Bragg gratings. A reduction of the resonant linewidth with respect to a conventional π-shifted Fiber Bragg grating and a fiber ring resonator, having the same physical parameters, is theoretically proved, achieving up to five orders of magnitude improvement with respect to the usual ring resonator. Due to these resonance features, the π-shifted Bragg grating ring resonator results suitable for RI sensing applications requiring extremely narrow resonances for high resolution measurements. In particular, by assuming a refractive index sensing to detect the presence of sugar in water, the sensor can show a theoretical resolution better than 10^{-9} RIU.

OCIS codes: (230.0230) Resonators; (130.6010) Integrated optics; (230.4555) Coupled resonators.

References and links

1. G. Gagliardi, M. Salza, S. Avino, P. Ferraro, and P. De Natale, "Probing the Ultimate Limit of Fiber-Optic Strain Sensing," Science **330**(6007), 1081–1084 (2010).
2. S. Avino, V. D'Avino, A. Giorgini, R. Pacelli, R. Liuzzi, L. Cella, P. De Natale, and G. Gagliardi, "Detecting ionizing radiation with optical fibers down to biomedical doses," Appl. Phys. Lett. **103**(18), 184102 (2013).
3. Q. Wu and Y. Okabe, "High-sensitivity ultrasonic phase-shifted fiber Bragg grating balanced sensing system," Opt. Express **20**(27), 28353–28362 (2012).
4. A. M. Gillooly, L. Zhang, and I. Bennion, "Quasi-distributed strain sensor incorporating a chirped Moire´ fiber Bragg grating," IEEE Photon. Technol. Lett. **17**(2), 444–446 (2005).
5. M. Pisco, A. Iadicicco, S. Campopiano, A. Cutolo, and A. Cusano, "Structured chirped fiber Bragg gratings," J. Lightwave Technol. **26**(12), 1613–1625 (2008).
6. I. Teraoka, "A hybrid filter of Bragg grating and ring resonator," Opt. Commun. **339**, 108–114 (2015).
7. K. McGarvey-Lechable and P. Bianucci, "Maximizing slow-light enhancement in one-dimensional photonic crystal ring resonators," Opt. Express **22**(21), 26032–26041 (2014).
8. C. E. Campanella, L. Mastronardi, F. De Leonardis, P. Malara, G. Gagliardi, and V. M. N. Passaro, "Investigation of fiber Bragg grating based mode-splitting resonant sensors," Opt. Express **22**(21), 25371–25384 (2014).
9. C. E. Campanella, F. De Leonardis, and V. M. N. Passaro, "Performance of Bragg grating ring resonator as high sensitivity refractive index sensor," IEEE Fotonica AEIT Italian Conference on Photonics Technologies 2014, pp. 1–4, May 12th-14th, 2014, Naples (Italy).

#233668 - $15.00 USD Received 3 Feb 2015; revised 28 Apr 2015; accepted 29 Apr 2015; published 22 May 2015

10. P. Malara, L. Mastronardi, C. E. Campanella, A. Giorgini, S. Avino, V. M. N. Passaro, and G. Gagliardi, "Split-mode fiber Bragg grating sensor for high-resolution static strain measurements," Opt. Lett. **39**(24), 6899–6902 (2014).
11. W. Liang, L. Yang, J. K. S. Poon, Y. Huang, K. J. Vahala, and A. Yariv, "Transmission characteristics of a Fabry-Perot etalon-microtoroid resonator coupled system," Opt. Lett. **31**(4), 510–512 (2006).
12. A. Watkins, J. Ward, Y. Wu, and S. N. Chormaic, "Single-input spherical microbubble resonator," Opt. Lett. **36**(11), 2113–2115 (2011).
13. A. B. Matsko, L. Maleki, A. A. Savchenkov, and V. S. Ilchenko, "EIT in resonator chains: similarities and differences with atomic media," 34th Winter Colloquium on the Physics of Quantum Electronics (PQE) 2004; January 4–8, 2004; Snowbird, UT; United States.
14. S. N. Chormaic, Y. Wu, and J. M. Ward, "Whispering gallery mode resonators as tools for non-linear optics and optomechanics," Proc. SPIE, Laser Resonators, Microresonators, and Beam Control XIV, doi:10.1117/12.906665 (2012).
15. C. Ciminelli, C. E. Campanella, F. Dell'Olio, and M. N. Armenise, "Fast light generation through velocity manipulation in two vertically-stacked ring resonators," Opt. Express **18**(3), 2973–2986 (2010).
16. Y. P. Miao, B. Liu, and Q. D. Zhao, "Refractive index sensor based on measuring the transmission power of tilted fiber Bragg grating," Opt. Fiber Technol. **15**(3), 233–236 (2009).
17. A. Iadicicco, A. Cusano, A. Cutolo, R. Bernini, and M. Giordano, "Thinned fiber Bragg gratings as high sensitivity refractive index sensor," IEEE Photon. Technol. Lett. **16**(4), 1149–1151 (2004).
18. W. Liang, Y. Y. Huang, R. Xu, R. K. Lee, and A. Yariv, "Highly sensitive fiber Bragg grating refractive index sensors," Appl. Phys. Lett. **86**(15), 151122 (2005).
19. K. Zhou, Z. Yan, L. Zhang, and I. Bennion, "Refractometer based on fiber Bragg grating Fabry-Pérot cavity embedded with a narrow microchannel," Opt. Express **19**(12), 11769–11779 (2011).
20. Q. Wu, Y. Semenova, B. Yan, Y. Ma, P. Wang, C. Yu, and G. Farrell, "Fiber refractometer based on a fiber Bragg grating and single-mode-multimode-single-mode fiber structure," Opt. Lett. **36**(12), 2197–2199 (2011).
21. C. E. Campanella, A. Giorgini, S. Avino, P. Malara, R. Zullo, G. Gagliardi, and P. De Natale, "Localized strain sensing with fiber Bragg-grating ring cavities," Opt. Express **21**(24), 29435–29441 (2013).
22. L. S. Grattan and B. T. Meggitt, *Optical Fiber Sensor Technology: Advanced Applications - Bragg Gratings And And Distributed Sensors* (Springer 2000).
23. A. Figotin and I. Vitebskiy, "Gigantic transmission band-edge resonance in periodic stacks of anisotropic layers," Phys. Rev. E Stat. Nonlin. Soft Matter Phys. **72**(3 Pt 2), 036619 (2005).
24. F. De Leonardis, C. E. Campanella, B. Troia, A. G. Perri, and V. M. N. Passaro, "Performance of SOI Bragg grating ring resonator for nonlinear sensing applications," Sensors (Basel) **14**(9), 16017–16034 (2014).
25. A. E. Miroshnichenko, S. Flach, and Yu. S. Kivshar, "Fano resonances in nanoscale structures," Rev. Mod. Phys. **82**(3), 2257–2298 (2010).
26. L. Y. Mario, S. Darmawan, and M. K. Chin, "Asymmetric Fano resonance and bistability for high extinction ratio, large modulation depth, and low power switching," Opt. Express **14**(26), 12770–12781 (2006).
27. M. Li, X. Wu, L. Liu, X. Fan, and L. Xu, "Self-referencing optofluidic ring resonator sensor for highly sensitive biomolecular detection," Anal. Chem. **85**(19), 9328–9332 (2013).
28. F. Vollmer and S. Arnold, "Whispering-gallery-mode biosensing: label-free detection down to single molecules," Nat. Methods **5**(7), 591–596 (2008).
29. F. Vollmer and L. Yang, "Label-free detection with high-*Q* microcavities: a review of biosensing mechanisms for integrated devices," Nanophotonics **1**(3-4), 267–291 (2012).
30. N. E. Fisher, D. J. Webb, C. N. Pannell, D. A. Jackson, L. R. Gavrilov, J. W. Hand, L. Zhang, and I. Bennion, "Ultrasonic hydrophone based on short in-fiber Bragg gratings," Appl. Opt. **37**(34), 8120–8128 (1998).
31. R. C. Astle and M. J. Weast, *Handbook of Chemistry and Physics*, 64th. ed. (CRC Press Inc., 1983).
32. N. Lin, L. Jiang, S. Wang, Q. Chen, H. Xiao, Y. Lu, and H. Tsai, "Simulation and optimization of polymer-coated microsphere resonators in chemical vapor sensing," Appl. Opt. **50**(28), 5465–5472 (2011).
33. C. Ciminelli, F. Dell'Olio, C. E. Campanella, and M. N. Armenise, "Numerical and experimental investigation of an optical high-Q spiral resonator gyroscope", International Conference on Transparent Optical Networks (ICTON), DOI: 10.1109/ICTON.2012.6254463, Coventry (United Kingdom) 2–5 July 2012.
34. W. Zhu, T. Shi, Z. Tang, B. Gong, G. Liao, and J. Tully, "Dynamic selective etching: a facile route to parabolic optical fiber nano-probe," Opt. Express **21**(6), 6919–6927 (2013).
35. F. Vollmer and H. G. L. Schwefel, "Taking detection to the limit with optical microcavities: recent advances presented at the 560. WE Heraeus Seminar," Europ. Phys. J. Sp. Top. **23**(10), 1907–1916 (2014).

1. Introduction

Although the commonly used high-resolution FBG sensors are based on Fabry-Perot configurations [1,2], other kinds of FBG structures, including π-phase shifted gratings [3], Moirè gratings [4] and chirped gratings [4,5], are more suited in certain applications where specific spectroscopic characteristics (i.e. narrow resonances) are required. If the spectral behavior of these grating based configurations and their physical principles are well-known in the frame of sensing applications, too, the possibility of combining these grating-based

#233668 - $15.00 USD Received 3 Feb 2015; revised 28 Apr 2015; accepted 29 Apr 2015; published 22 May 2015

devices with standard ring resonators and the physical behaviors deriving from this hybridization is one field that merits to be further explored. These hybrid devices have been already identified such as add-drop filters [6] while the guidelines for a band edge slow light magnification together with a Q-factor enhancement have been also presented [7]. These configurations have been yet proposed and investigated in terms of splitting mode devices for enhanced sensing applications in the context of strain sensors [8,9]. The experimental validation of an enhanced resolution strain sensor based on these hybrid resonant architectures has been reported in [10], confirming the advantages offered from mode splitting resonant configurations.

Thus, if these devices show a splitting mode resonant behaviour (i.e. one effect properly belonging to the coupled resonant systems), the ability to give rise to other physical effects is typically expected (i.e., zero transmission [11], Fano-type transmission [12], electromagnetically-induced-transparency (EIT)-like transmission [13], electromagnetically-induced-absorption (EIA)-like transmission [14], fast and slow light effects [15], etc..), as demonstrated for other resonant coupled systems. Indeed, in this paper we show that, by tayloring the geometry and the physical characteristics of the device [8], the splitting dynamics can be modified in order to generate a Fano-type narrow linewidth transmission profile. Apart the intriguing demonstration of this effect, the advantage offered from a spectroscopic point of view in refractive index (RI) sensing applications will be highlighted. Indeed, because in the last decade Fiber Bragg gratings (FBGs) have assumed considerable importance for RI sensing applications [16–20] due to their small sizes, low cost, high resolution, immunity to electromagnetic interferences, and possibility of directly embedding into the structures, the employment of the narrow Fano resonance can be extremely important with the aim of improving the sensing resolution. In particular, the proposed RI sensor consists of a ring resonator cavity made by enclosing a π-shifted Fiber Bragg grating on itself through a supplementar optical path which introduces an overall phase delay of π between the two counter-propagating waves. The device is excited by an optical coupler 1 and the optical electric field is extracted by a fiber coupler 2. The RI sensitive region (π-region) is obtained by removing the fiber cladding from a conventional single mode fiber (SMF). The paper is organized as follows. In Section II we theoretically describe the physical effects involved in the physical behaviour (i.e. Fano type transmission) of the π-shifted Fiber Bragg Grating Ring Resonator (π-FBGRR), showing that this configuration allows to achieve better performance in terms of linewidth reduction not only with respect to the commonly used π-shifted Bragg gratings, but also to the standard ring resonators. In Section III we explain how these physical effects can be exploited for RI sensing applications, evaluating the improved performance of the proposed sensor. Section IV summarizes the conclusions.

2. Resonant features of the π-Bragg grating in closed loop

The π-shifted Fiber Bragg Grating Ring Resonator (π-FBGRR) is sketched in Fig. 1 and has been already proposed and modelled in [8], where an additional conventional fiber path has been used to close the loop. It is physically composed from one FBG closed on itself through an additional optical path which introduces a phase delay (Φ) for each counter-propagating wave generated inside the ring cavity [21]. This phase delay can be expressed like in [8], as:

$$\Phi = \frac{\pi}{2}\frac{\lambda_B}{\lambda} = \frac{2\pi n_{eff(d)}}{\lambda}\frac{\Lambda_B}{2} \tag{1}$$

where $n_{eff(d)}$ is the effective index of the optical mode propagating through the defect of length $\Lambda_B/2$ (with Λ_B the FBG period) in the (d) defective region, called π in Fig. 1. The sensitive element of the RI sensor is represented by this defective region, as shown in the yellow inset of Fig. 1. This solution has been proposed with reference to another structure [18], where a chemical removal (i.e., etching) of the fiber cladding (see the inset of Fig. 1) is applied to a

#233668 - $15.00 USD Received 3 Feb 2015; revised 28 Apr 2015; accepted 29 Apr 2015; published 22 May 2015

standard SMF in order to increase the evanescent field interaction with the surrounding environment. This technique allows the precise control of the etching position and diameter [18]. The spectral response of the device, T, derived as in [8], can be expressed by a general closed form analytical expression:

$$T = \left|\frac{E_o}{E_{in}}\right|^2 = \left|\frac{1}{2}\left[\frac{k^2 a\left(t^2 e^{j\Phi} + r\left(t^2 - \left(r^2+1\right)\right)\right)}{\left(r^2+1\right) - \tau^2 a^2\left(t^2 e^{j\Phi} + r\left(t^2 - \left(r^2+1\right)\right)\right)} + \frac{k^2 a\left(t^2 e^{j\Phi} - r\left(t^2 - \left(r^2+1\right)\right)\right)}{\left(r^2+1\right) - \tau^2 a^2\left(t^2 e^{j\Phi} - r\left(t^2 - \left(r^2+1\right)\right)\right)}\right]\right|^2 \quad (2)$$

where τ and k are the fractions of the optical amplitudes transmitted and coupled via the evanescent couplers 1 and 2, respectively, t and r the electrical field amplitudes transmitted and reflected by the FBG, respectively, given by:

$$t = \frac{\Theta}{\Theta\cos\mathrm{h}(\Theta\ell) + j\Delta\beta\sin\mathrm{h}(\Theta\ell)}; \qquad r = \frac{jK\sin\mathrm{h}(\Theta\ell)}{\Theta\cos\mathrm{h}(\Theta\ell) + j\Delta\beta\sin\mathrm{h}(\Theta\ell)} \quad (3)$$

where $|t|^2 + |r|^2 = 1$, in the ideal case of loss-less FBG, being ℓ the half length of the FBG, and Θ, K and $\Delta\beta$ can be expressed as:

$$\Theta = \left[\left|K\right|^2 - \left(\Delta\beta\right)^2\right]^{\frac{1}{2}}; \qquad K = \frac{\pi\left|\Delta n\right|}{\lambda_B}; \qquad \Delta\beta = 2\pi n_{eff}\left(\frac{\lambda_B - \lambda}{\lambda\lambda_B}\right) \quad (4)$$

with n_{eff} the effective index of the fiber mode, $|\Delta n|$ and λ_B the grating index modulation depth and the Bragg wavelength (i.e., $\lambda_B = 2n_{eff}\Lambda_B$, with Λ the FBG period), respectively. In Eq. (2), a is an attenuation coefficient equal to $\exp(-\alpha\ell)$, where α is the fiber propagation loss for unit length and ℓ is the half length of the cavity geometrical path (i.e., the half length of the π-FBG). The assumption of a loss-less FBG has been proved to be valid for weak index modulation depth (i.e., $|\Delta n| \le 5 \times 10^{-4}$) [10, 21], and, thus, for these values $a \to 1$. In fact, the loss associated with the multiple reflections at the interfaces is negligible for gratings with very moderate index modulation (i.e., moderate UV intensities to create the Bragg grating onto the fiber, with index contrast $< 5 \times 10^{-4}$) [22]. Anyway, the same considerations are still valid for a standard π-FBG where the attenuation of the transmission resonance at the Bragg wavelength is negligible, still in the assumption of moderate index modulation depths ($< 5 \times 10^{-4}$). The right hand side of Eq. (2) is a combination of two "symmetric" and "antisymmetric" guided wave solutions, as widely discussed in [8]. However, differently from [8], in the proposed architecture of Fig. 1 the standard fiber path linking the two π-FBG ends is not present, and the π-FBG ring resonator is simply formed by a π-FBG in closed loop.

To describe the physical behavior of the device, we consider the physical parameters in Table 1 with reference to the model in [8], whose values are usual in fiber optics technology. In particular, the excitation and extraction fibers are typical single mode fibers (SMF), while the π-FBGRR parameters are those usually used in manufacturing the FBGs (i.e. $\lambda_B = 1.5605$ μm with a $|\Delta n|$ in the range of $10^{-5} \div 5 \times 10^{-4}$). In a first step, we consider the defective region as a normal SMF, without any cladding removal (i. e., $n_{eff} = n_{eff(d)}$).

#233668 - $15.00 USD Received 3 Feb 2015; revised 28 Apr 2015; accepted 29 Apr 2015; published 22 May 2015

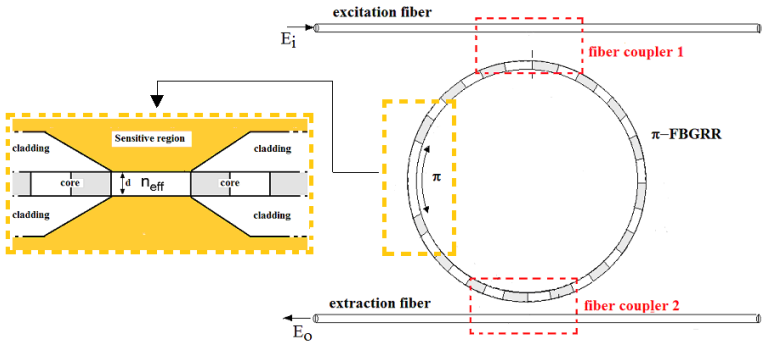

Fig. 1. π-shifted Fiber Bragg Grating Ring Resonator (π-FBGRR) obtained by enclosing on itself a FBG through an additional optical path which introduces an overall phase delay of π between the two counter-propagating waves. The device is excited by an optical coupler 1 and the optical electric field is extracted by a fiber coupler 2. (Inset) Sensitive region (π-region), where the fiber cladding has been removed from the standard SMF. $n_{eff(d)}$ is the effective index assumed by the optical mode propagating through the π-region, changing due to an external substance.

Table 1. Physical parameters and assumed values.

Parameters	Assumed values
n_{eff} (SMF)	1.457
$n_{eff(d)}$ (defective region)	1.457 (in absence of any fiber cladding removal)
λ_B (Si)	1.5605 μm
Λ_B (SiO_2)	535.5 nm
ℓ (SiO_2)	2 cm
α_{loss}	0.45×10^{-5} m^{-1}
	0.15 ÷ 0.95 (Fig. 2)| 0.95 (dotted curve), 0.975 (solid curves) (Figs. 3 and 4)
	0.175 ÷ 0.999 (solid curve) (Fig. 5)
k	$(1-\tau^2)^{1/2}$

With the same values assumed as in Table 1, the spectral responses (T) for the usual Ring Resonator RR, Fig. 2(a), the Fiber Bragg Grating Ring Resonator FBGRR, Fig. 2(b), and π-FBGRR, Fig. 2(c), are reported in Fig. 2 for comparison. In particular, the spectral responses of the three different devices have been evaluated by varying τ from 0.15 to 0.95, with a step of 0.2. In Eq. (2)-(4), $|\Delta n| = 0$ and $\Phi = 0$ have been assumed for RR and FBGRR, respectively.

In Fig. 2(b), FBGRR is characterized by a symmetric spectral behavior, showing transmission resonances placed at the FBG band edge oscillations. These resonances hold a mirror symmetry with respect to the Bragg wavelength. By increasing τ from 0.15 to 0.95, only the transmission resonances associated to those spectral oscillations for which the transmission of the FBG is almost equal to 1, are allowed. Moreover, symmetrically displaced around λ_B, narrow resonance linewidths occur at the band edges (spectral points where the argument of Θ is real with reference to [8]). These band edges resonances [23], forming a splitting doublet, lie at λ^* and λ^{**} [24] as:

$$\lambda^* = \frac{2n_{eff}}{2n_{eff} + |\Delta n|}\lambda_B; \quad \lambda^{**} = \frac{2n_{eff}}{2n_{eff} - |\Delta n|}\lambda_B \tag{5}$$

and in Fig. 2(b) they are very close to 1.56048 μm and 1.56052 μm, respectively. Due to the strong structural dispersion, occurring when the Bragg condition is satisfied, the band edge resonances have a linewidth narrower than the others. Moreover, as shown in Fig. 2(c), by introducing a phase mismatch $\Phi = \pi$ between the two counter-propagating waves inside the

#233668 - $15.00 USD Received 3 Feb 2015; revised 28 Apr 2015; accepted 29 Apr 2015; published 22 May 2015

ring cavity, the spectral mirror symmetry is removed. On the other hand, this phase mismatch is also responsible for the removal of the degeneracy of the FBGRR resonances. Indeed, in the π-FBGRR spectrum this leads to the formation of a couple of resonances, instead of a single resonance in the FBGRR. This couple is composed by a left side resonance, characterized by a symmetric profile and described by a Lorentzian function, and a right side resonance having an asymmetric profile.

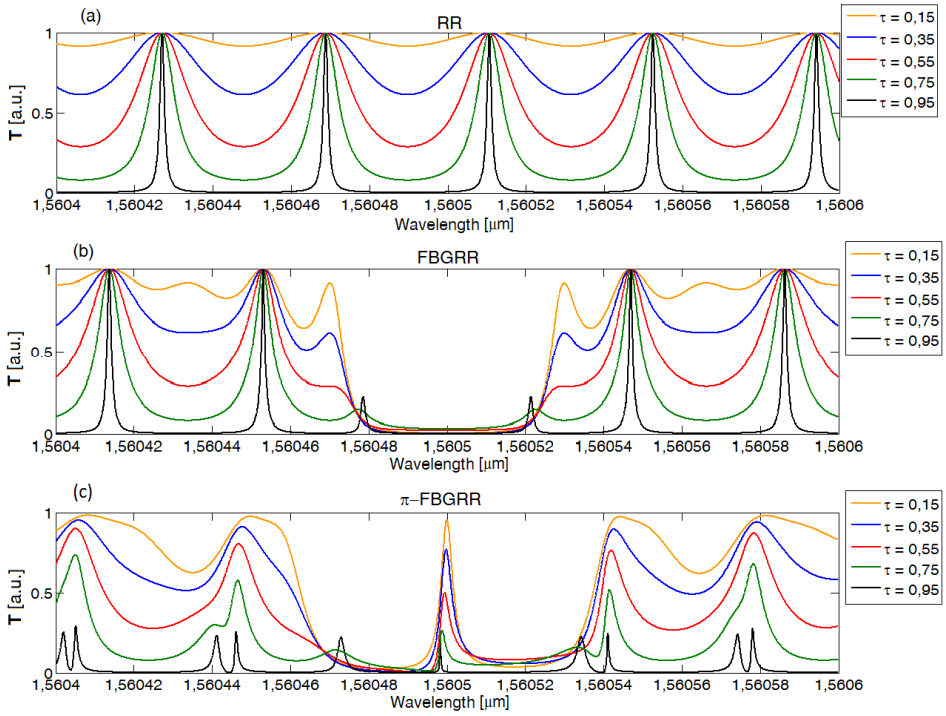

Fig. 2. Spectral responses (T), evaluated with the parameters reported in Table 1, when τ is varied from 0.15 to 0.95 with a step of 0.2 for: (a) RR ($|\Delta n| = 0$ in Eq. (2)); (b) FBGRR ($\Phi = 0$ in Eq. (2)); (c) π-FBGRR ($|\Delta n| = 4 \times 10^{-5}$ in Eq. (2)).

The latter resonance shows a narrower and sharper peak than all the other kinds of resonances achievable with these configurations. By comparing the π-FBGRR spectral response for $\tau = 0.95$ (black curve in Fig. 2(c)) with that of the RR having the same physical and geometrical parameters (black curve in Fig. 2(c)), this asymmetric resonance is seen to be about four times narrower than the RR resonance. In fact, due to its sharpness and asymmetrical nature, the origin of this resonance is attributed to the Fano-Feshbach effect [25,26], arising from the close coexistence of resonant transmissions and reflections. In other words, this effect results from the interference between direct and indirect resonance-assisted pathways, as due to the scattering inside the optical cavity. To better explain the Fano-Feshbach resonance effect, in Fig. 3(b) for $\tau = 0.95$ (dotted curve) and $\tau = 0.975$ (all the solid curves) we consider the π-FBGRR transmission spectrum compared with that of the typical π-FBG (i.e., not closed to form a ring resonator). As can be easily seen in Fig. 3(a), the π-FBG is characterized by a single transmission resonance (i.e. one localized allowed resonance state) lying at λ_B and surrounded by a reflection band (a continuum of not allowed propagation states), associated to the fulfillment of the Bragg condition in a spectral range approximatively equal to [λ*, λ**]. In Fig. 3(a), the Fano resonance around 1.5605 μm shows a spectral linewidth more than twenty times narrower than the π-FBG transmission resonance in Fig. 3(b), at 1.5605 μm. By analyzing Fig. 3(a), it is clear that so as the transmission resonance linewidth is reduced with the increase of the index modulation depth from 1×10^{-5}

#233668 - $15.00 USD Received 3 Feb 2015; revised 28 Apr 2015; accepted 29 Apr 2015; published 22 May 2015

to 4×10^{-5}, as the reflection band is enlarged. Otherwise, by considering the spectral portion on the right side of λ_B for the π-FBGRR in Fig. 3(b), the couple of transmission resonances behaves like an asymmetrical split doublet, with a splitting magnitude increasing when $|\Delta n|$ is increased. In particular, for this variation of $|\Delta n|$ a blue-shift of the left side Lorentzian resonance and a red-shift of the right side Fano resonance simultaneously occur.

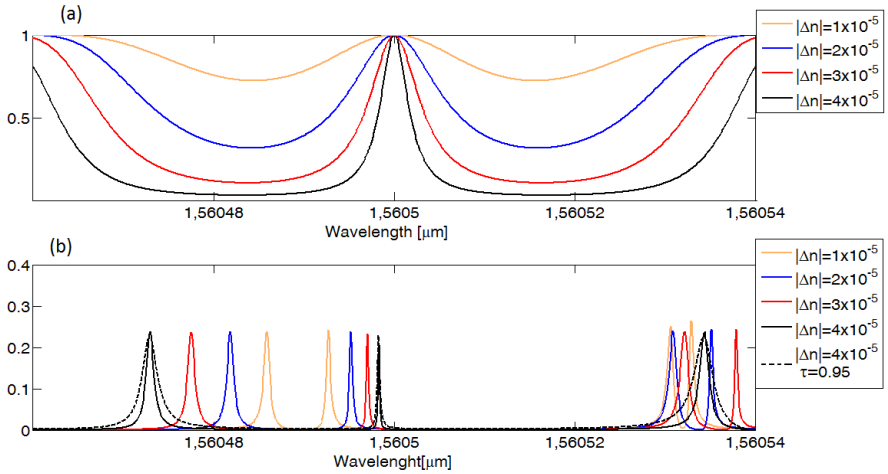

Fig. 3. Spectral responses (*T*), evaluated with the parameters reported in Table 1: (a) π-FBG; (b) π-FBGRR, where the dotted curve is obtained for $\tau = 0.95$ (as in Fig. 2). The solid curves are evaluated for $\tau = 0.975$ with $|\Delta n|$ varying from 1×10^{-5} to 4×10^{-5} with a step of 1×10^{-5}.

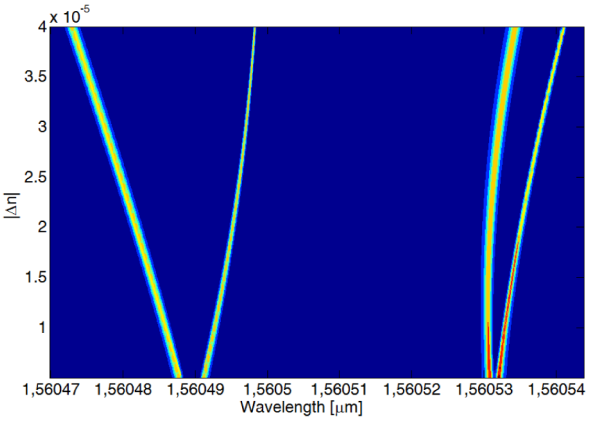

Fig. 4. Transmission (T) contour curve evaluated by changing $|\Delta n|$ from 5×10^{-6} to 4×10^{-5} with a step of 1×10^{-6} in the [1.56047 μm ÷ 1.56054 μm] λ-range, being $\tau = 0.975$.

As it can be deduced by comparing Fig. 3(b) with Fig. 3(a), the Fano resonance lies on that wavelength corresponding to the left side of the half maximum of π-FBG transmission peak. Together with this opposite shift, the resonance linewidths suffer of a similar opposite behavior because the left side Lorentzian resonance linewidth is enlarged, while simultaneously the right side Fano resonance linewidth is reduced. It is interesting to notice that, together with this opposite behavior in terms of shift and linewidth variation, the asymmetry between these two resonances is characterized by a similar opposite behavior, too. In fact, by increasing $|\Delta n|$ the asymmetry of the right side Fano resonance is enhanced while the left side resonance tends to be much more symmetrical (i.e., it tends to preserve the Lorentzian shape). The transmission contour curve in Fig. 4, obtained by increasing $|\Delta n|$ from

#233668 - $15.00 USD Received 3 Feb 2015; revised 28 Apr 2015; accepted 29 Apr 2015; published 22 May 2015

5×10^{-6} to 4×10^{-5} with a step of 1×10^{-6} in the λ-range [1.56047 μm ÷ 1.56047 μm], helps to better explain these effects.

Due to the change of $|\Delta n|$, a splitting magnitude variation, associated to the asymmetrical split doublet (i.e., composed by a Lorentzian and a Fano resonance), occurs. In fact, in the curve two asymmetrical split doublets are reported. In particular, for the splitting doublet closest to the Bragg wavelength (i.e., where the π-FBG resonance lies), the splitting magnitude variation is enhanced with respect to that of the other split doublet (i.e., that associated to the band edge oscillation of π-FBG). Now, with the purpose of comparing the linewidth associated with the Fano resonance with the Lorentzian one of a typical RR, the resonance linewidths variation as a function of τ have been numerically calculated in the spectral range around λ_B for two values of $|\Delta n|$ (i.e. 5×10^{-5} and 2×10^{-4}) and are sketched in Fig. 5.

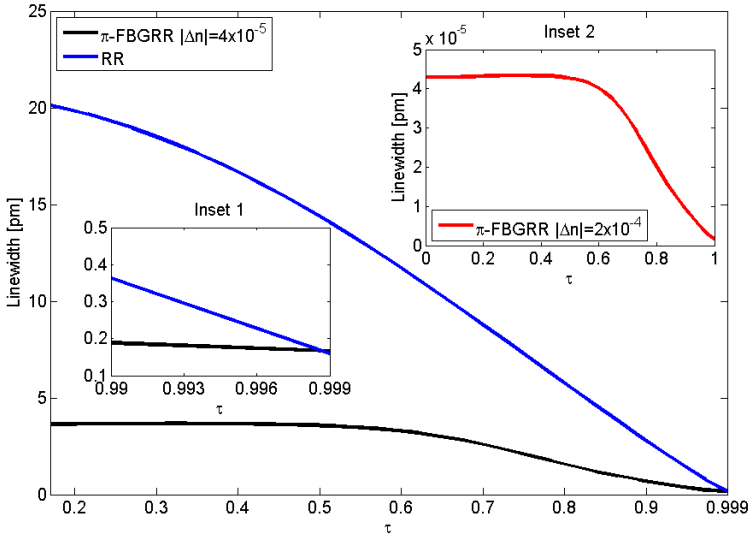

Fig. 5. Linewidth curve evaluated by changing τ from 0.175 to 0.999, near λ_B, for typical RR (blue curve), π-FBGRR with $|\Delta n| = 4 \times 10^{-5}$ (black curve), and π-FBGRR with $|\Delta n| = 2 \times 10^{-4}$ (red curve in the inset 2).

When τ is varied in the range [0.175 ÷ 0.999], the π-FBGRR shows a resonant linewidth (black curve in Fig. 5 for $|\Delta n| = 5 \div 10^{-5}$) reduced of about 4.5 times in the τ-range [0.2 ÷ 0.6] and more flat with respect to that in RR (i.e., corresponding to $|\Delta n| = 0$, blue curve in Fig. 5). The black and blue curves cross each other for τ = 0.999, as can be seen in the inset 1 of Fig. 5. Otherwise, as shown by the red curve in the inset 2 of Fig. 5, when $|\Delta n| = 2 \times 10^{-4}$ the π-FBGRR linewidth is about five orders of magnitude narrower than in the simple RR, with a flat behaviour similar to that one of the black curve. Moreover, the simulations confirm that the Fano resonance is suppressed within the PBG of π-FBGRR for $|\Delta n| > 3 \times 10^{-4}$ because, as can be seen in Fig. 4, the Fano resonance close to 1.56049 tends to be reduced when the index modulation depth (i.e. $|\Delta n|$) is increased until that value of $|\Delta n| > 3 \times 10^{-4}$ for which the Fano resonance is impossible to be distinguished. In other words, the proposed device simultaneously shows the advantages associated to the splitting effect and the Fano resonance linewidth reduction, with important improvements if used for sensing applications. Thus, this physical effect can be thought like an asymmetrical splitting effect showing not only the advantage that could be exploited in sensing applications requiring low sensitivity to the noise due to the external perturbations [21, 27–29], but also in those sensing applications requiring very narrow and sharp resonance linewidths [1, 30].

#233668 - $15.00 USD Received 3 Feb 2015; revised 28 Apr 2015; accepted 29 Apr 2015; published 22 May 2015

3. RI sensing performance of π-Bragg grating in closed loop

Once the physics of the device has been explained, in this section we focus on the possibility of exploiting the advantages offered from the Fano resonance linewidth reduction for RI sensing applications. To this aim, with reference to the structure reported in Fig. 1, we consider a π-FBGRR with $|\Delta n| = 2 \times 10^{-4}$ whose linewidth is about five orders of magnitude narrower than the usual RR. We evaluated the SMF effective index ($n_{eff(d)}$) in the defective region by considering the SMF core diameter (d in Fig. 1) of 8.2 μm. Indeed, in Fig. 6 by using the Finite Element Method we have evaluated the effective index ($n_{eff(d)}$) at 1.55 μm in the sensitive region by considering a cladding index (n_{cl}) variation with a step of 0.05 RIU, ranging from 1 (air) to 1.4564 (silicon dioxide of fiber cladding). This range includes different refractive indices of substances that can be analyzed by RI sensors, such as 1.025 (helium), 1.33 (water), 1.38 (alcohol) 1.42 (50% of sugar in water), as shown in Fig. 6. The evaluated values of $n_{eff\ (d)}$ have been fitted by using the analytical expression reported in Eq. (6) in the mentioned range. Indeed, the double weighted exponential formula in Eq. (6) approximates the values obtained by FEM with a very small error, less than 5%:

$$n_{eff\,(d)}(n_{cl}) = ae^{(bn_{cl})} + ce^{(dn_{cl})} \tag{6}$$

where a = 1.4525 and $c = 1.645 \times 10^{-18}$, $b = 7.996 \times 10^{-4}$ and d = 23.9 are the fitting parameters of exponential functions which vary with n_{cl}. The blue dotted curves are the confidence bounds for which the estimate values are over or under the 5% of the fitting curve.

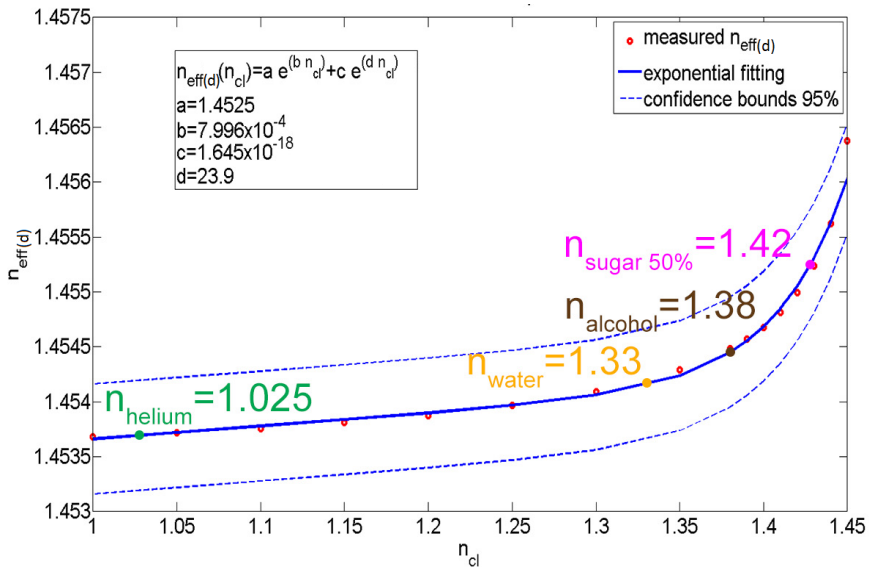

Fig. 6. Effective index ($n_{eff(d)}$) near 1.55 μm in the defective region (i.e., π-region in Fig. 1) by considering a cladding index variation as 1 (air), 1.025 (helium), 1.33 (water), 1.38 (alcohol) 1.42 (50% of sugar in water) and 1.4564 (silicon dioxide of the standard fiber cladding).

It is clear that, when n_{cl} increases, the core/cladding index contrast is reduced and, in its turn, the fundamental optical mode propagating through the defective region is less confined. This means that the overlapping of evanescent field with the substance to be analyzed is enhanced by the exponential law of Eq. (6). As expected [18], the reflection spectra for the open loop π-FBG will be shifted depending on the substance placed in the defective etched region, due to the interaction with the environment. In turn, the Fano resonance will also suffer from one shift, depending on the environmental substance. Being the interaction length very short (i.e., Λ), the absorption loss due to the presence of the substance can be neglected

#233668 - $15.00 USD Received 3 Feb 2015; revised 28 Apr 2015; accepted 29 Apr 2015; published 22 May 2015

and the linewidth of the Fano resonance is very slightly modified. Indeed, in Fig. 7, by numerically evaluating the Fano resonance wavelength from Eq. (2), we report the Fano resonance shift (i.e. $\Delta\lambda = \lambda_{F,substance} - \lambda_{F,air}$), evaluated as the difference between the Fano resonance wavelength when $n_{cl} = n_{substance}$ (i.e., $\lambda_{F,substance}$) and the Fano resonance wavelength when $n_{cl} = n_{air}$ (i.e., $\lambda_{F,air}$, assumed as the reference resonance wavelength) as a function of n_{cl} (i.e., the same considered in Fig. 6 due to the presence of the different substances in the sensing area). The behavior of $\Delta\lambda$ as a function of n_{cl} can be also approximated with a precision of 95% by using the approximating exponential curve, plotted in Fig. 7, and reported in the following expression:

$$\Delta\lambda(n_{cl}) = ae^{(bn_{cl})} \tag{7}$$

where $a = 1.331 \times 10^{-14}$ μm and $b = 11.41$. This, in turn, means that the wavelength shift as a function of n_{cl} is not a linear function for large variations of n_{cl}, as expected from the previous discussion about the evanescent field interaction with the substance to be analyzed. For the simulations reported in Fig. 7, the maximum variation of the Fano resonance linewidth with n_{cl} is less than the 1%, i.e. this influence is negligible.

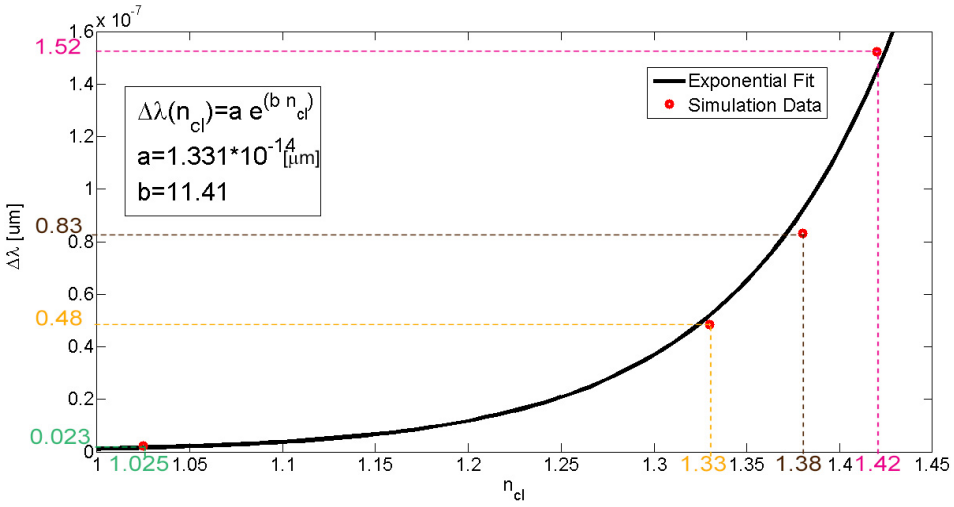

Fig. 7. Fano resonance shift (i.e. $\Delta\lambda = \lambda_{F,substance} - \lambda_{F,air}$), as a function of the values assumed from n_{cl}.

With the purpose of evaluating the performance of the proposed sensor, we have considered as test solution that one composed by a varying percentage of sugar dissolved in water. As reported in Fig. 8(a), n_{cl} varies from 1.332 RIU to 1.505 RIU with a sugar concentration from 0% to 85%, respectively [31]. Due to the variation of n_{cl}, associated to the change of the sugar concentration, the $n_{eff(d)}$ change is responsible of a $\Delta\lambda$ change from 0.05 pm (0% sugar in water) to 0.375 pm (85% sugar in water), as sketched in Fig. 8(b). The sensitivity of the device, referred to the test solution, has been evaluated as:

$$S_{nc} = \frac{\partial\lambda_F}{\partial n_{cl}} \tag{8}$$

and reported in Fig. 9(a).

As expected, the sensitivity reported in Fig. 9(a) shows a nonlinear behavior depending on the exponential behavior of $n_{eff(d)}(n_{cl})$ and on the chemistry of the detected solution, whose behavior is reported in Fig. 8(a)-(b). The sensitivity, depending on the initial chosen sugar concentration, is improved going toward highest values of the sugar concentration. This

#233668 - $15.00 USD Received 3 Feb 2015; revised 28 Apr 2015; accepted 29 Apr 2015; published 22 May 2015

means that, by considering an initial value of sugar concentration in water, the sensor can linearly operate by detecting small variations of the sugar concentration around this initial value.

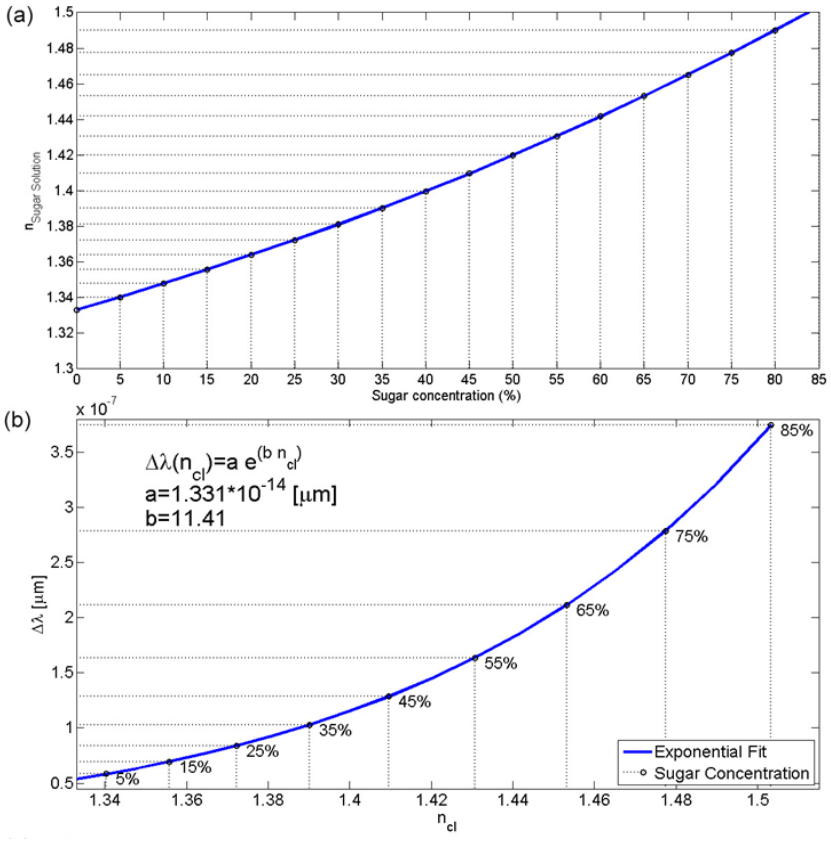

Fig. 8. (a) n_{cl} as function of sugar concentration in water; (b) Fano resonance shift as a function of the values assumed from n_{cl}, due to different concentrations of sugar in water.

Once the sensitivity is known, we can evaluate the minimum detectable cladding index as:

$$\partial n_{cl\min} = \frac{n_{eff(d)}}{\lambda}\left(\frac{\partial n_{eff(d)}}{\partial n_{cl}}\right)^{-1} \times FWHM_{Fano} \tag{9}$$

where $FWHM_{Fano}$ is the linewidth associated with the Fano type resonance, strongly improved with respect to the usual ring resonator, as demonstrated in the previous section. Indeed, in Fig. 9(b), a minimum detectable cladding index going from 1.75×10^{-9} RIU (small sugar concentration in water) to 0.5×10^{-10} RIU (high sugar concentration in water) has been evaluated. These values represent a significant improvement with respect to the best theoretical values reported in literature (i.e., 10^{-8} RIU [32] for a silica microsphere), using a different sensor architecture. The read-out technique appropriate for this sensor is based on an indirect characterization consisting on the wavelength scan of a narrow linewidth laser, with a resolution limited only by the laser linewidth [11, 33]. The method for manufacturing the π-FBGRR consists in the splicing of the two ends of an open loop π-FBG, so forming a closed loop π-FBG. Then, the closed loop π-FBG is evanescently coupled with two conventional fibers in order to build the two couplers. After that, appropriate cladding removal of π-FBG in the defective region is required [18]. To this purpose, very accurate etching methods, allowing

#233668 - $15.00 USD Received 3 Feb 2015; revised 28 Apr 2015; accepted 29 Apr 2015; published 22 May 2015

the control of very short lengths like the phase shifted region, have been proved [34]. For framing the proposed sensor in the state-of-the-art of RI sensors, a performance comparison with other con urations can be done [35]. Moreover, these considerations, although referred to a homogeneous sensing mechanism, able to detect the presence of different sugar concentrations in water, can be extended to other kinds of substances to be analyzed or to other sensing mechanisms.

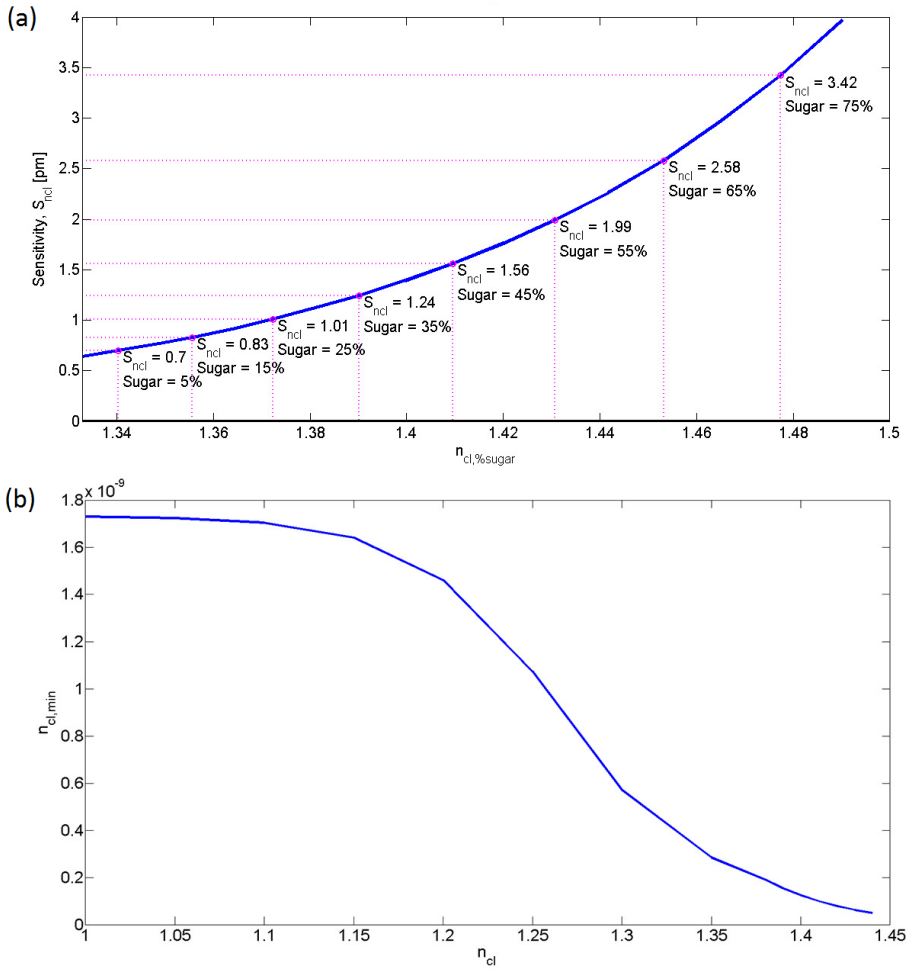

Fig. 9. (a) Sensor sensitivity; (b) Sensor resolution (i.e., minimum detectable n_{cl}).

4. Conclusions

A theoretical investigation of a ring resonant cavity obtained by closing on itself a π-shifted fiber Bragg grating to be used for RI sensing applications, has been reported. The cavity spectrum is characterized by an asymmetric splitting doublet composed by a left side resonance, having a symmetric profile and described by a Lorentzian function, and by a right side resonance having an asymmetric Fano profile. The latter resonance shows a peak narrower and sharper than all the other kinds of resonance achievable with both conventional ring resonators and π-shifted fiber Bragg gratings. For specific parameters, the resonant linewidth can be reduced until to five orders of magnitude with respect to a conventional ring resonator. Due to these improved resonance features, the π-shifted Bragg grating ring resonator results suitable for RI sensing applications requiring extremely narrow resonances

#233668 - $15.00 USD Received 3 Feb 2015; revised 28 Apr 2015; accepted 29 Apr 2015; published 22 May 2015

to obtain high accuracy measurements. Indeed, if we suppose to monitor the sugar concentration in water, a minimum detectable cladding index (i.e., sensor resolution) going from 1.75×10^{-9} RIU (small sugar concentration in water) to 0.5×10^{-10} RIU (high sugar concentration in water) has been evaluated. These resolution values, although referred to a homogeneous sensing mechanism, can be extended to other kinds of substances to be analyzed as well as to other sensing mechanisms.

Acknowledgments

This work has been partially supported by Politecnico di Bari under Fondo Ricerca di Ateneo (FRA) 2012 funding scheme.

#233668 - $15.00 USD Received 3 Feb 2015; revised 28 Apr 2015; accepted 29 Apr 2015; published 22 May 2015